Laser & Photonics Reviews

LASER & PHOTONICS REVIEWS

www.lpr-journal.org

RESEARCH ARTICLE

Broadband III-V/Lithium Niobate Actively Mode-Locked Lasers

Xujia Zhang[1] | Yuyao Guo[1] | Xiaotian Xue[2] | Tianyi Li[1] | Zekun Cui[1] | Hao Li[2] | Xianfeng Chen[2] | Yuanlin Zheng[2] | Jianping Chen[3] | Kan Wu[1]

[1]State Key Laboratory of Micro-Nano Engineering Science, School of Information Science and Electronic Engineering, Shanghai Jiao Tong University, Shanghai, China | [2]State Key Laboratory of Photonics and Communications, School of Physics and Astronomy, Shanghai Jiao Tong University, Shanghai, China | [3]State Key Laboratory of Photonics and Communications, School of Information Science and Electronic Engineering, Shanghai Jiao Tong University, Shanghai, China

Correspondence: Yuyao Guo (guoyuyao1992@sjtu.edu.cn) | Kan Wu (kanwu@sjtu.edu.cn)

Received: 17 July 2025 | **Revised:** 11 January 2026 | **Accepted:** 12 January 2026

Keywords: hybrid integration | lithium niobate | mode-locked laser | optical frequency comb

ABSTRACT

Chip-scale optical frequency combs (OFCs) enable integrated solutions for various applications among optical communications, LiDAR, spectroscopy, and radio frequency signal generation. Among integrated OFC platforms, III-V semiconductor mode-locked lasers provide gigahertz repetition rates but often suffer from limited power and tunability due to narrow driving current ranges. Hybrid integration with thin-film lithium niobate (TFLN) has been explored to address these limitations, but previous III-V/TFLN mode-locked lasers exhibited narrow spectral widths, constrained by gain bandwidth and cavity dispersion. This work demonstrates broadband III-V/TFLN integrated actively mode-locked lasers at the telecom band, leveraging a broadband multiple-quantum-well reflective semiconductor optical amplifier (RSOA). A mode-locked laser with a high-reflectivity TFLN mirror generates a 45-nm-span spectrum with a 10-dB bandwidth of 19.1 nm and a beat-note contrast exceeding 60 dB, while another laser with a low-reflectivity RSOA output facet achieves an off-chip output power of 26 mW with a 10-dB bandwidth of 11.4 nm. Numerical simulations based on the Haus's master equation and the generalized nonlinear Schrödinger equation confirm the role of slight inhomogeneous gain in supporting stretched-state pulse solutions and overcoming dispersion-limited spectral narrowing. This work demonstrates outstanding spectral performance and provides a promising route toward broadband, high-power OFC sources for integrated photonic applications.

1 | Introduction

Optical frequency combs (OFCs), consisting of a series of evenly spaced and coherent spectral lines, serve as a stable and precise bridge between optical and radio frequencies (RF). Since their emergence, OFCs have demonstrated transformative potential in a wide range of fields, including optical communication [1–3], optical frequency synthesizers [4, 5], ranging [6–8], comb spectroscopy [9, 10], astronomical detection [11, 12], integrated photonic computing [13, 14], and the generation of ultrastable microwave signals [15, 16]. Recent progress in integrated photonic platforms has enabled the realization of chip-scale OFC sources. In comparison with conventional tabletop comb systems, integrated solutions offer substantial improvements in compactness, power consumption, and stability, which significantly enhance the potential for the practical deployment and large-scale implementation of OFCs in a wide range of applications such as navigation and remote sensing [17]. Moreover, optical microcombs typically operate at repetition rates ranging from gigahertz to terahertz, far exceeding those of conventional counterparts, which makes them uniquely suited for applications like optical communications [18].

As chip-scale OFCs advance from proof-of-concept demonstrations to practical application deployment, their spectral characteristics have become key determinants of system performance, particularly in high-capacity optical communication and microwave photonic systems, where the comb's spectral bandwidth directly influences the number of usable channels as well as the frequency achievable in RF signal generation and processing. Consequently, the realization of stable mode-locked integrated OFCs with spectral spans ranging from tens to hundreds of nanometers has become a pivotal research frontier in integrated photonics.

Integrated OFCs can be realized through two main technological approaches: Kerr frequency combs rely on nonlinear optical processes in high-Q microresonators, which typically require high pump power and complex soliton-trapping dynamics [19]. Chip-scale ultrafast mode-locked lasers, which integrate mode-locking mechanisms within the cavity to directly generate gigahertz-repetition-rate pulse trains with intrinsically equidistant comb spectra, offer an alternative approach to integrated OFCs. In particular, owing to their higher output power and greater integration level compared with Kerr microcombs, chip-scale mode-locked lasers demonstrate remarkable potential for power-intensive applications such as dense wavelength-division multiplexing and optical interconnects [20–23]. III-V semiconductor gain media have been widely adopted in integrated mode-locked lasers due to their high optical gain and high saturation power. Early work centered on monolithic multi-section III-V devices that realized passive mode locking via an integrated saturable-absorber section, which was typically an active region operated under reverse bias [24]. With the pursuit of higher performance and the continuous advancement of fabrication technologies, hybrid integration has become a major topic of investigation. III-V gain chips have been integrated with external cavities based on a variety of low-loss platforms such as silicon [25–28], silicon nitride [29–32], and other material systems through approaches including direct growth [25, 27], butt-coupling [30], and micro-transfer printing [29, 31]. Researchers have demonstrated low-noise mode-locked lasers enabled by external-cavity feedback [28–31]. Although passive mode locking remains the most widely employed strategy [33], its stable operation is typically confined to a narrow window of driving current and reverse bias voltage, which inherently limits the tunability and output power of integrated mode-locked lasers.

Recently, hybrid integration platforms combining reflective semiconductor optical amplifiers (RSOAs) with thin-film lithium niobate (TFLN) have attracted significant interest, as they leverage the high gain of RSOAs along with the efficient electro-optic modulation capability of TFLN to provide ideal conditions for actively mode-locked laser operation [34, 35]. An electrically pumped actively mode-locked laser based on an RSOA and an external TFLN cavity has been demonstrated, generating optical pulses with a repetition rate of approximately 10 GHz and a central wavelength around 1065 nm [34]. Nevertheless, the optical spectrum has been limited to approximately 5 nm due to limitations in the gain bandwidth and cavity dispersion. The spectrum can be broadened by exploring the Kerr effect in a ring resonator with feedback locking, enabling a ~45-nm-wide mode-locked microcomb, but this requires precise dispersion engineering of the waveguide and complex electrical feedback control [35].

In this work, we report hybrid III-V/TFLN phase-modulated mode-locked lasers that achieve broadband spectral coverage and high fiber-coupled power. Our design leverages the intrinsic coexistence of homogeneous and inhomogeneous gain in a broadband InGaAsP multiple-quantum-well (MQW) RSOA to access a stretched-state solution predicted by Haus's master equation (HME). By integrating the RSOA with the TFLN chip through a spot-size converter, we demonstrate two complementary cavity configurations to achieve broadband optical spectra and high output power. The mode-locked laser with LN-side output (LN-MLL) employs high-reflectivity mirrors on both the TFLN chip and the RSOA chip to realize broadband comb generation, while the mode-locked laser with RSOA-side output (RSOA-MLL) incorporates a low-reflectivity output mirror on the RSOA chip to enhance off-chip power. These designs optimize the performance of integrated III-V/TFLN actively mode-locked lasers and reveal the significant potential of broadband mode-locked lasers for applications in data communications, LiDAR, and spectroscopic sensing.

2 | Principles

The mode-locking mechanism of the phase-modulated mode-locked laser is depicted in Figure 1a. When the phase modulation frequency is matched to the free spectral range (FSR), the sidebands of each longitudinal mode generated through phase modulation can be efficiently injected into adjacent modes, enabling intermodal phase synchronization and resulting in a periodic pulse train in the time domain. Phase-modulation-induced spectral broadening is ultimately limited by the gain bandwidth, establishing a frequency-domain equilibrium that supports the generation of a stable mode-locked laser. In the absence of dispersion and nonlinearity, pulses can form at either of the two extrema of the modulation cycle, and experimental observations have shown that the mode-locked pulse train randomly switches between the two temporal locations [36]. The opposite directions of instantaneous frequency variation introduced by the phase modulator at the two extrema result in pulses with opposite chirp signs. In the presence of cavity dispersion, the same chirp sign from the dispersion and the phase modulation leads to pulse stretching, whereas an opposite chirp sign results in pulse compression. The pulse in the stretched state exhibits a broader optical spectrum but experiences greater loss due to gain filtering, causing the laser to preferentially operate in the compressed state, where the spectrum is narrower, and the loss is lower [37]. However, when an inhomogeneous gain distribution exists, frequency-selective amplification can provide higher net gain for the broader-spectrum laser, enabling the stretched state to become a new steady operating point. In this section, we verify this behavior through theoretical analysis and numerical simulations.

When nonlinear effects are neglected, the dynamic evolution of a phase-modulated mode-locked laser can be described by HME [38, 39], which is expressed as:

$$T_{\mathrm{R}}\frac{\partial A(T,t)}{\partial T}=\left[g(T)-l+(D_{\mathrm{g}}+iD)\frac{\partial^2}{\partial t^2}\pm iM\cos(\omega_{\mathrm{m}}t)\right]A(T,t) \tag{1}$$

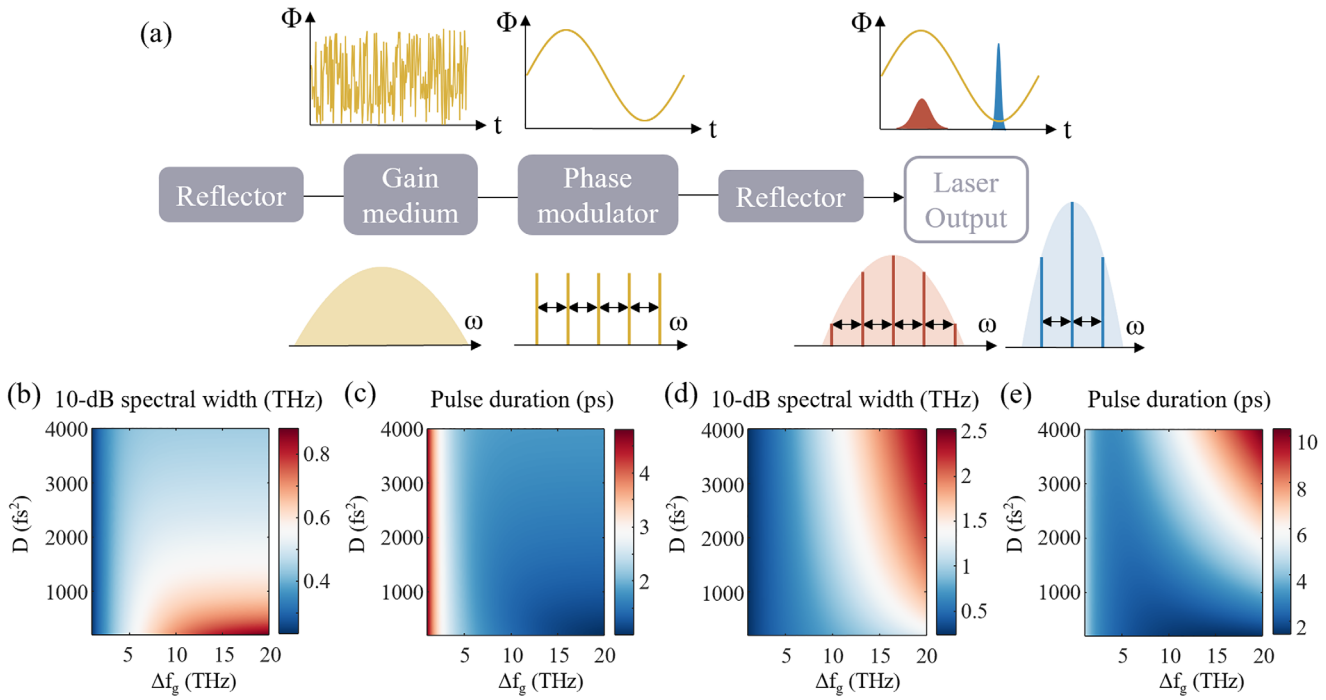

FIGURE 1 | (a) Schematic and mode-locking mechanism of the phase-modulated mode-locked laser. (b) 10-dB spectral bandwidth and (c) temporal duration of the pulses in the compressed state within a normal-dispersion cavity when $M = \pi, f_m$ = FSR = 6.8 GHz, $l = 0.98$. (d) 10-dB spectral bandwidth and (e) temporal duration of the pulses in the stretched state within a normal-dispersion cavity when $M = \pi, f_m$ = FSR = 6.8 GHz, $l = 0.98$.

here, T_R denotes the round-trip time of the laser cavity. $g(T)$ represents the gain coefficient, and l represents the loss coefficient. $D_g = g/(\pi\Delta f_g)^2$ accounts for the gain dispersion, where Δf_g denotes the 3-dB gain bandwidth. D represents half of the round-trip group delay dispersion (GDD) of the cavity. $M = \pi V_{pp}/V_\pi$ denotes the modulation depth of the phase modulator. $\omega_m = 2\pi f_m$ is the angular frequency of the phase modulation. $A(T,t)$ describes the evolution of the pulse envelope as a function of the slow time $T \gg T_R$ and the fast time $t \ll T_R$.

Assuming a steady-state solution in the form of a chirped Gaussian pulse, the analytical expression for the 10-dB spectral bandwidth $\Delta f_{10\text{-dB}}$ of the mode-locked laser can be derived as follows:

$$\Delta f_{10-\mathrm{dB}} = \frac{\sqrt{2\ln 10}}{\pi}\left[\frac{D^2 + D_g^2 \pm D\sqrt{D^2 + D_g^2}}{D_g}\right]^{\frac{1}{2}} \times \left[\frac{M\omega_m^2}{4(D^2 + D_g^2)(\sqrt{D^2 + D_g^2} \pm D)}\right]^{\frac{1}{4}} \quad (2)$$

According to Equation (2), we draw the pulse temporal duration and 10-dB spectral bandwidth in a normal-dispersion cavity depending on the cavity dispersion D and the gain bandwidth Δf_g. Figure 1b,c present the characteristics of pulses in the compressed state, highlighting that the opposite chirp sign introduced by dispersion and phase modulation causes detuning between the modulation frequency and the cavity mode spacing, which in turn limits the spectral broadening achievable with increasing gain bandwidth. As a consequence, achieving broadband performance in the compressed state requires careful dispersion engineering. In contrast, Figure 1d,e show the characteristics of pulses in the stretched state, where the spectral bandwidth increases with the gain bandwidth without being constrained by dispersion, which enables broadband comb generation. The pulse duration, however, is limited by both the gain bandwidth and cavity dispersion, resulting in relatively broad chirped pulses. Both the spectral bandwidth and pulse duration scale with one-fourth power of the modulation depth M, thus being weakly affected by it.

To illustrate the pulse formation mechanisms at different temporal positions and the intracavity field evolution dynamics, we numerically solve Equation (1) using the split-step Fourier method. Considering gain saturation and the combined homogeneous and inhomogeneous broadening of the gain medium, the intracavity gain can be expressed as:

$$G(f) = (1-\alpha)\, g_{\mathrm{homo}} g_{\mathrm{shape}}(f) + \alpha g_{\mathrm{inho}}(f) \quad (3)$$

Here, $\alpha \in [0,1]$ describes the proportion of the inhomogeneous gain component. $g_{\mathrm{shape}}(f)$ is the normalized Gaussian function used to limit the gain bandwidth Δf_g. The homogeneous gain component $g_{\mathrm{homo}} = g_0/(1+P_{\mathrm{av}}/P_{\mathrm{sat}})$ distributes the total available gain uniformly across the entire frequency range, where g_0 denotes the small-signal gain coefficient, and P_{sat} represents the total saturation power. In contrast, the frequency-selective inhomogeneous gain component follows a local saturation model, $g_{\mathrm{inho}}(f) = g_0 g_{\mathrm{shape}}(f)/[1+P(f)/P_{\mathrm{sat}}(f)]$, where $P(f)$ denotes the spectral power at a specific frequency.

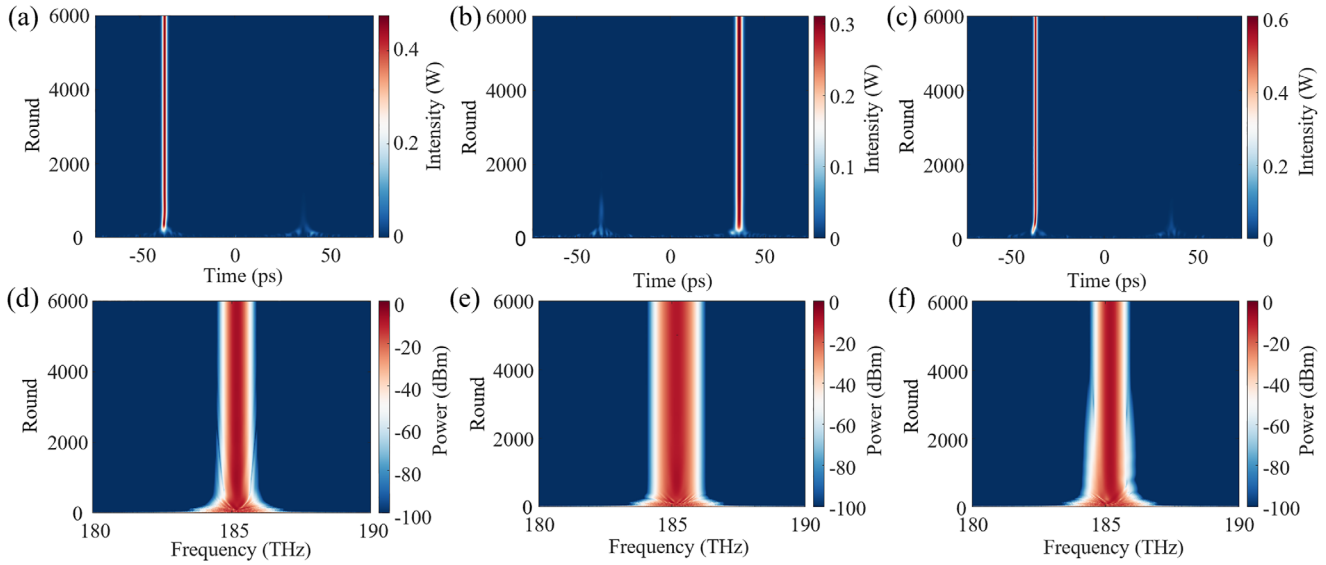

FIGURE 2 | Numerical simulation of pulse formation from noise. (a–c) Temporal and (d–f) spectral evolutions of the intracavity field under different gain inhomogeneity conditions. (a,d) Results for $\alpha = 0$, representing purely homogeneous gain. (b,e) Results for $\alpha = 1.5\%$, with the laser operating at the stretched-state extremum of the phase modulation cycle. (c,f) Results for $\alpha = 1.5\%$, with the laser operating at the compressed-state extremum. The simulation parameters for (b,e) and (c,f) are identical except for the initial noise.

The temporal and spectral evolutions of the intracavity field corresponding to the case with purely homogeneous gain (i.e., $\alpha = 0$) are shown in Figure 2a,d, respectively. After the initial noise evolves over 3000 round-trips, a mode-locked pulse spontaneously always forms at the pulse compression state due to the higher loss experienced by the broader spectral components under gain filtering. When a small fraction of inhomogeneous gain is introduced, e.g., $\alpha = 1.5\%$, the intracavity dynamics undergo significant changes: the mode-locked laser can randomly operate at either the stretched-state (see Figure 2b,e) or compressed-state (see Figure 2c,f) extrema of the phase modulation cycle. These two states are obtained under identical simulation conditions, with the final results determined by the initial noise. Pulses in the stretched state exhibit significantly broader temporal and spectral bandwidths compared to those in the compressed state. The additional amplification provided by the inhomogeneous gain to the broader spectral components compensates for the gain filtering loss of comb lines away from the central frequency, and helps overcome the intrinsic limitation of purely homogeneous-gain media, in which narrowband spectra tend to exhibit lower intracavity loss. Supported by the frequency-selective amplification of the inhomogeneous gain, the stretched state can achieve a net gain comparable to or even greater than that of the compressed state and consequently stabilizes as an alternative steady-state solution.

3 | Experiment and Results

In a InGaAsP MQW RSOA, a broadband homogeneous background gain naturally coexists with inhomogeneous broadening arising from microscopic variations in quantum well thickness, material composition, and interface quality [40, 41], as well as nonlinear gain effects induced by spectral hole burning [42], resulting in the mixed-gain spectrum. The integrated actively mode-locked lasers consist of a 1-mm-long RSOA directly butt-coupled to a TFLN nanowaveguide through a spot size converter, with a simulated coupling loss of approximately 1.3 dB. Two laser configurations are investigated in our experiment. The LN-MLL delivers laser output from the TFLN chip to facilitate broader comb generation, while the RSOA-MLL outputs the laser from the low-reflectivity facet of the RSOA chip to achieve higher output power.

Figure 3a shows the schematic of the LN-MLL. A Sagnac loop mirror on the TFLN chip serves as a broadband reflector with approximate 70% reflectivity, forming a Fabry–Pérot (FP) cavity with the high-reflectivity facet of the RSOA chip, resulting in an FSR of 6.8 GHz. The laser output is emitted from the TFLN chip, with the output waveguide tilted at 20° to suppress Fresnel reflection at the LN-air interface. The coupling loss between the LN nanowaveguide and the optical fiber is approximately 7 dB/facet. Photographs of the device and the coupling region are shown in Figure 3b, where the RSOA facet is butt-coupled to the TFLN waveguide via an index-matching liquid ($n \approx 1.414$) to reduce interface reflections. The amplified spontaneous emission (ASE) spectra of the RSOA are measured without an external reflector, as shown in Figure 3c. The oscillations observed at the top of the ASE spectra result from weak reflection at the coupling fiber facet. At a driving current of 100 mA, the 3-dB bandwidth reaches approximately 75 nm. When the current increases to 260 mA, the 3-dB bandwidth extends beyond 100 nm.

A broadband mode-locked laser is generated by driving the phase modulator using an external RF signal whose frequency is matched to the FSR of the cavity. The RF power is set to be 30 dBm, corresponding to a modulation depth of approximately $M \approx \pi$. At a driving current of 100 mA, the optical spectrum of the mode-locked laser is shown in Figure 3d. A magnified view of the comb structure is provided in the inset, highlighting the detailed features of the uniformly distributed comb lines. The time-domain pulse train is measured using an

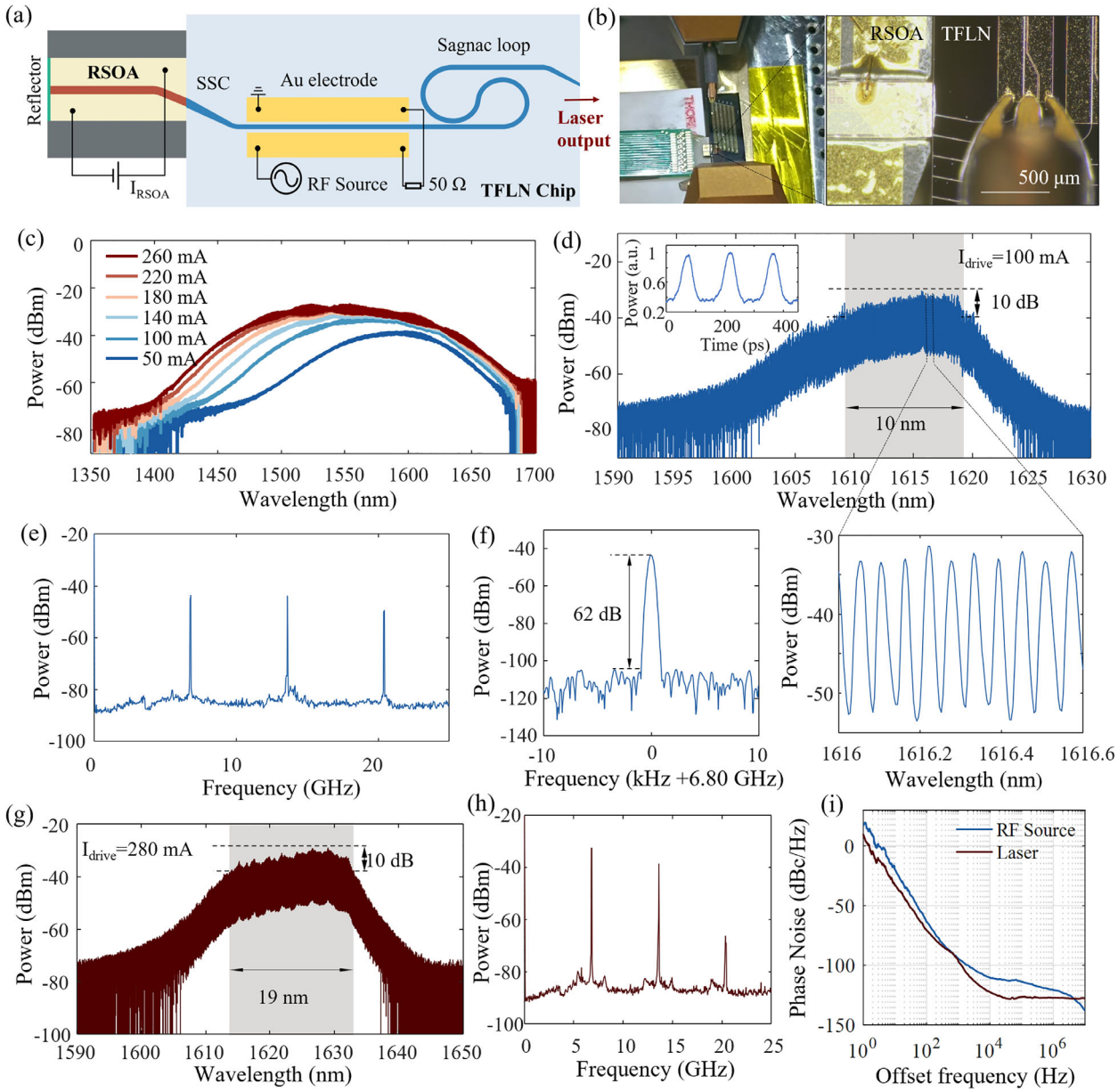

FIGURE 3 | (a) Schematic of the broadband actively mode-locked laser (LN-MLL). (b) Experimental photograph of the mode-locked laser. Inset: the photo of the coupling region. (c) Amplified spontaneous emission (ASE) spectra of the RSOA measured under free-running conditions without an external reflector at different driving currents. (d) Optical spectrum of the LN-MLL at a driving current of 100 mA, with a 10-dB bandwidth of 9.8 nm. Inset: time-domain pulse train measured by an optical sampling oscilloscope of 500 GHz bandwidth. Zoom-in: detailed spectral structure with uniformly spaced optical modes. (e) Electrical spectrum of the beat note at a driving current of 100 mA (RBW: 50 kHz). (f) Narrow-span electrical spectrum at a driving current of 100 mA (RBW: 200 Hz). (g) Optical spectrum of the laser at a driving current of 280 mA, with a 10-dB bandwidth of 19.1 nm. (h) Electrical spectrum of the beat note at a driving current of 280 mA (RBW: 30 kHz). (i) Single-sideband phase noise of the RF source and the beat note of the laser.

optical sampling oscilloscope of 500 GHz bandwidth (Alnair-lab, EYE2000C), as shown in the inset of Figure 3d. The spectrum spans approximately 30 nm, featuring a 10-dB bandwidth of 9.8 nm that contains 164 comb lines. The off-chip output power is 0.94 mW. The electrical spectrum is detected using a high-speed photodetector (PD) and an electrical spectrum analyzer (ESA), as shown in Figure 3e, revealing the fundamental beat note at 6.80 GHz along with the second and third harmonics. The fundamental beat note exhibits a high signal-to-noise ratio (SNR) of 62 dB, as illustrated in Figure 3f, clearly indicating the establishment of a stable mode-locked state with sustained stability over an extended observation period. When the driving current is increased to 280 mA, the optical spectrum is centered at 1625 nm, spanning 45 nm in total, with a 10-dB bandwidth of 19.1 nm that contains 318 comb lines, as shown in Figure 3g. The off-chip output power reaches 2.4 mW. The electrical spectrum measured by ESA, as shown in Figure 3h, clearly exhibits peaks at the fundamental frequency and its second and third harmonics. The single-sideband phase noise (SSB-PN) of the fundamental RF beat note and that of the RF source are measured

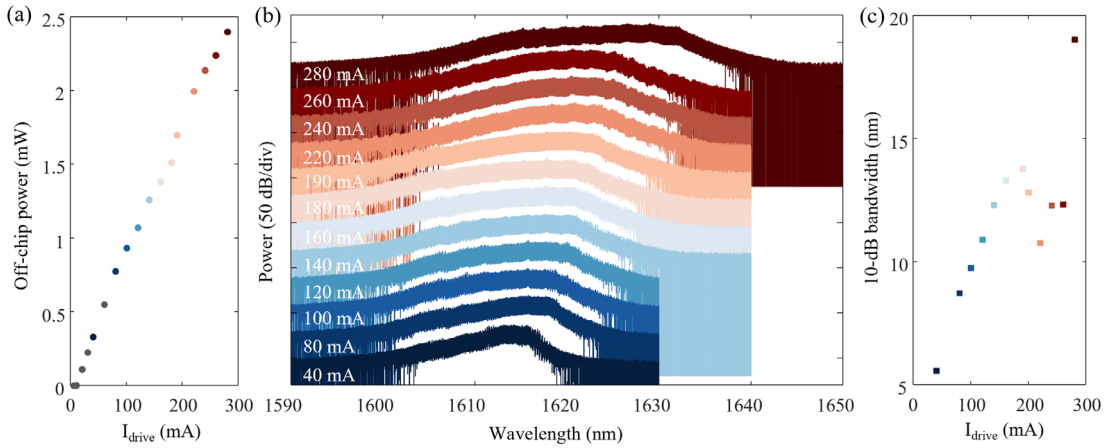

FIGURE 4 | (a) Measured off-chip output power with respect to driving currents, indicating a threshold current of 20 mA. (b) Laser output spectra at various driving currents. (c) 10-dB spectral bandwidth of the laser spectra at various driving currents.

using an ESA (R&S FSUP50), as shown in Figure 3i. The SSB-PN is dominated by the RF source but is reduced at certain frequencies by the filtering effect of the actively mode-locked laser [43].

The off-chip output power depending on the driving current is shown in Figure 4a, with the laser exhibiting a threshold current of 20 mA. As the driving current increases, the 10-dB spectral bandwidth broadens from 5.6 nm at 40 mA to 19.1 nm at 280 mA, accompanied by a redshift of the spectral center from 1613 to 1625 nm, as shown in Figure 4b,c. The increase in spectral bandwidth is primarily attributed to the expansion of the gain bandwidth with increasing current and temperature. However, at driving currents of 190, 200, 230, and 250 mA, the 10-dB bandwidth deviates from the general trend, which may be caused by coupling-state variations between the two chips due to thermal expansion and vibrations. This deviation remains under investigation. The observed redshift of the lasing wavelength relative to the ASE spectrum arises from carrier clamping near threshold, which maintains a lower carrier density during lasing [44, 45]. The lasing spectral redshift with increasing driving current is primarily attributed to localized temperature rise [40]. In terms of the central wavelength, bandgap engineering of the RSOA can shift the gain spectrum toward shorter wavelengths, enabling lasing near 1550 nm. As the driving current increases, the laser operation gradually becomes unstable due to mechanical instability induced by enhanced thermal effects. By packaging the chip on a thermally stabilized platform to mitigate these effects, lasers with broader optical spectra and higher output powers can be achieved.

Moreover, lowering the TFLN mirror reflectivity can enhance output power but increase the intracavity loss, thereby reducing the achievable spectral bandwidth and compromising the laser stability. During the establishment of the mode-locked state, phase-modulated light from the TFLN chip is injected into the RSOA to facilitate phase synchronization among longitudinal modes. As the phase-modulated light experiences propagation loss within the TFLN nanowaveguide and coupling loss at the TFLN-RSOA interface, further reduction of the reflectivity on the TFLN chip may result in insufficient feedback power, making it difficult to suppress perturbations, for example, reflections occurring at the TFLN-RSOA interface, thereby hindering the formation of a stable mode-locked state. Accordingly, we further developed the RSOA-MLL based on a low-reflectivity FP cavity, where a high reflectivity is preserved at the TFLN chip to ensure sufficient feedback, while the RSOA facet is coated with a low-reflectivity film (~6%) to enable efficient laser output.

The structure of the RSOA-MLL is schematically illustrated in Figure 5a. An external RF driving signal matched to the FSR of the cavity is applied to the phase modulator to generate a stable actively mode-locked laser. At a driving current of 300 mA, the optical spectrum spans from 1608 to 1635 nm, with a 10-dB spectral bandwidth of 11.4 nm and an off-chip output power of 26 mW, as shown in Figure 5b. Correspondingly, a beat note at 6.10 GHz is detected from the beating between the comb lines, as shown in Figure 5c, exhibiting an SNR of 48 dB, which indicates the establishment of a mode-locked comb state. The measured SSB-PN, illustrated in Figure 5d, closely matches that of the RF source without introducing additional noise, indicating high coherence in the laser emission. Moreover, Figure 5e presents the variation of the off-chip average output power as a function of the driving current, showing a threshold current of 30 mA. Figure 5f,g illustrate the output optical spectra and the corresponding 10-dB spectral bandwidths, respectively, measured at driving currents ranging from 100 to 300 mA, demonstrating spectral broadening and redshift characteristics similar to those observed in the LN-MLL. The periodic modulation observed on top of the spectra is attributed to FP cavity interference, which arises from localized reflections introduced by fabrication imperfections in the device.

The RSOA-MLL incorporates a low-reflectivity output mirror to boost output power, while enhanced coupling efficiency at the output facet further increases the optical power delivered into the fiber. TFLN nanowaveguides typically feature widths of 1–2 μm and thicknesses below 1 μm, which are poorly matched to the 2–-3 μm mode-field diameter of lensed fibers, resulting in fiber-to-chip coupling losses of 6–-9 dB/facet without spot-size converters. Edge coupler designs can significantly reduce coupling loss but often rely on multilayer waveguide structures that increase fabrication complexity [46–49]. In contrast, RSOA waveguides exhibit larger mode sizes, enabling coupling losses

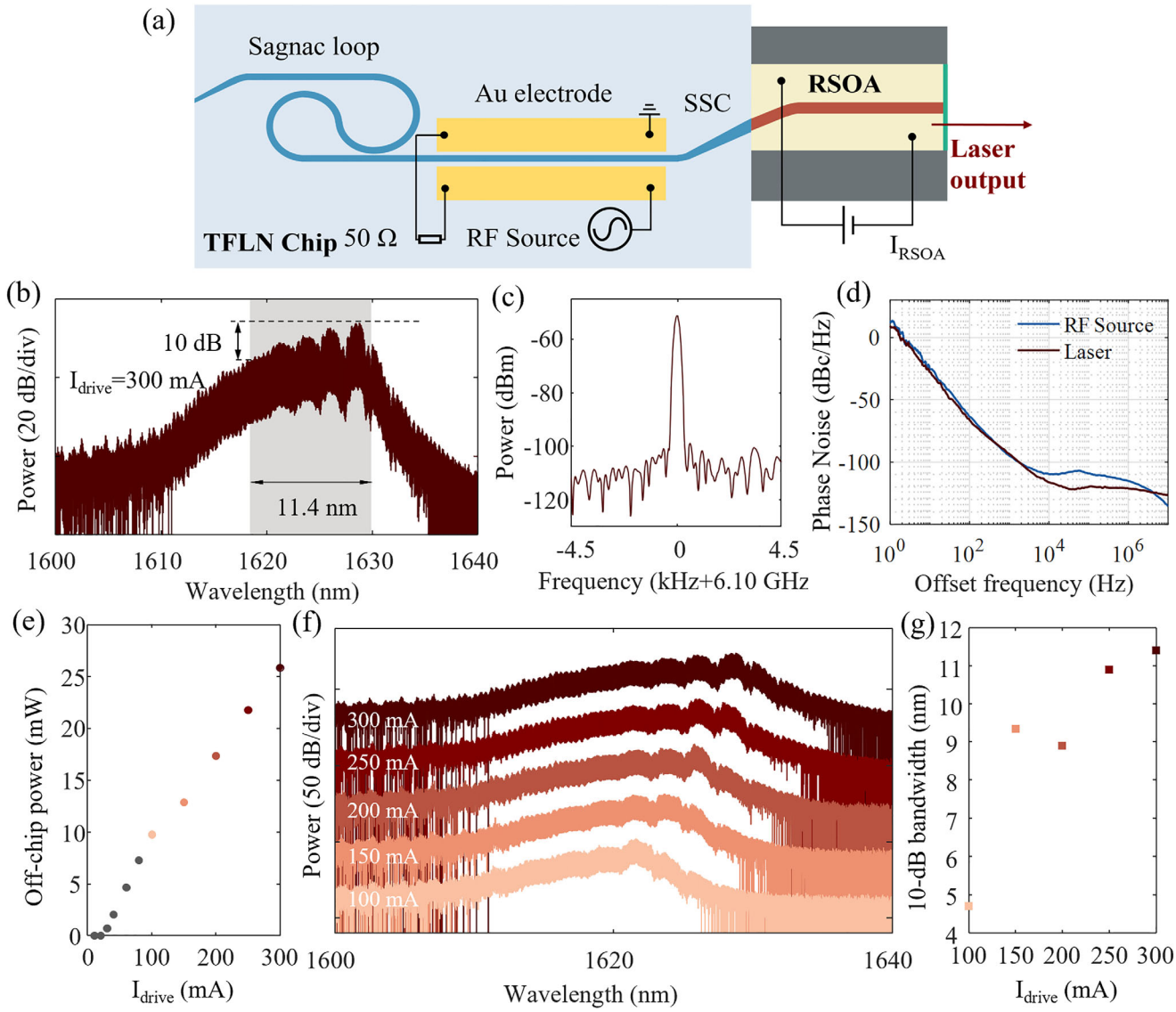

FIGURE 5 | (a) Schematic of the high power and broadband actively mode-locked laser (RSOA-MLL). (b) Optical spectrum of the laser at a driving current of 300 mA, with a 10-dB bandwidth of 11.4 nm. (c) Electrical spectrum of the beat note at a driving current of 300 mA. (d) Single-sideband phase noise of the RF source and the beat note of the laser. (e) Measured off-chip output power with respect to driving currents, indicating a threshold current of 30 mA. (f) Laser output spectra at various driving currents. (g) 10-dB spectral bandwidth of the laser spectra at various driving currents.

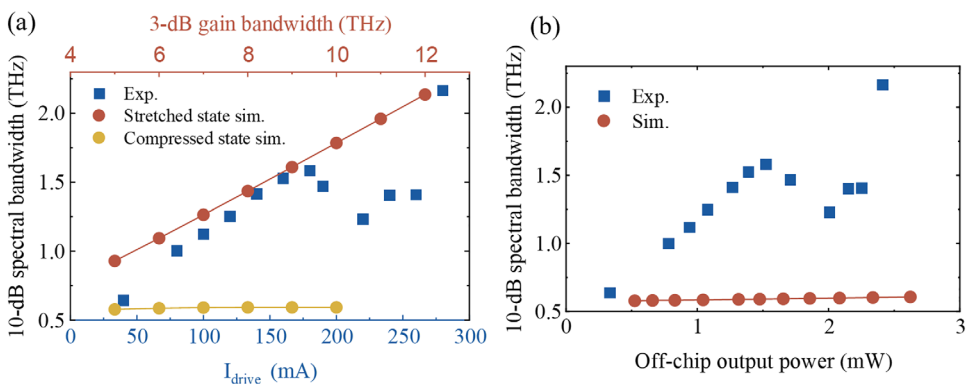

FIGURE 6 | (a) 10-dB spectral bandwidth obtained from both experimental measurements and numerical simulations as a function of driving current. The simulations account for inhomogeneous gain but exclude Kerr nonlinearity. (b) Relationship between 10-dB spectral bandwidth and off-chip output power from both experimental measurements and numerical simulations. The simulations account for Kerr nonlinearity but exclude inhomogeneous gain.

as low as ∼2 dB/facet. The use of a low-reflectivity mirror and laser emission from the RSOA facet enables higher fiber-coupled output power, offering increased power margin and enhanced system performance for integrated mode-locked lasers in applications such as high-capacity coherent communications, microwave photonic signal processing, and precision optical frequency comb metrology.

4 | Discussion

To further investigate the impact of various intracavity effects, we developed a numerical model based on the generalized nonlinear Schrödinger equation (GNLSE), closely reflecting the actual experimental system. The intracavity optical field sequentially propagates through the modeled components to complete a full cavity round-trip, iteratively repeating until a self-consistent steady-state solution is obtained, from which the stable mode-locked pulse characteristics are analyzed. Specifically, the simulation accounts for the dispersion, propagation loss in the TFLN nanowaveguides, gain in the RSOA, electro-optic phase modulation, mirror loss, and interface coupling loss between the RSOA and TFLN chips.

The simulation is performed using the estimated parameters of the LN-MLL. The intracavity effects governing the spectral bandwidth of the mode-locked laser are primarily the gain bandwidth and Kerr nonlinearity whose respective contributions are investigated through two sets of numerical simulations, as shown in Figure 6a,b. The spectral characteristics of the mode-locked laser at the two operating points are shown in Figure 6a. When the pulse forms at the pulse-stretched position, the optical spectrum broadens significantly with increasing gain bandwidth, with the 10-dB spectral width expanding from 0.9 to 2.1 THz as the gain bandwidth increases from 5 to 12 THz. In contrast, the comb spectrum formed at the pulse-compressed position remains limited by dispersion, with its 10-dB bandwidth increasing only slightly from 0.58 to 0.59 THz. These results are consistent with the trends observed in Figure 1b,d. Self-phase modulation (SPM), another well-known mechanism affecting spectral broadening, is further included into the model. The SPM contributions from the TFLN and RSOA segments are considered separately in the model, considering their different Kerr nonlinear coefficients and peak powers caused by coupling loss. The Kerr nonlinear coefficient n_2 is set to 1.8×10^{-19} m^2 W^{-1} for TFLN and -2×10^{-17} m^2 W^{-1} for the RSOA [50]. Further increases in n_2 for the RSOA lead to non-convergence of the numerical solution. In the absence of inhomogeneous gain, the simulated spectral bandwidths shown in Figure 6b indicate that the optical spectrum broadens slightly with increasing intracavity power. This limited broadening is primarily attributed to the normal dispersion in the TFLN nanowaveguides. Although some spectral broadening occurs within the RSOA segment, it is subsequently compressed in the TFLN nanowaveguide due to its normal dispersion. The longer interaction length of the TFLN nanowaveguide, combined with the peak power reduction caused by coupling losses at the RSOA-TFLN interface, further suppresses the spectral broadening effect of SPM. The experimentally observed spectral broadening with increasing driving currents is primarily attributed to the broadening of the gain bandwidth, rather than to SPM effects.

The differences between simulation and experimental results may arise from uncertainties in parameter estimation, such as the accurate modeling of inhomogeneous gain, the Kerr nonlinearity, the dispersion of the RSOA, and the carrier dynamics in the RSOA that are not included in the model, which are difficult to measure reliably in experiments. Despite these limitations, the simulation provides meaningful qualitative insight into the influence of the gain spectrum on the spectral characteristics of phase-modulated actively mode-locked lasers.

5 | Conclusion

In conclusion, we have demonstrated hybrid III-V/TFLN phase-modulated mode-locked lasers that achieve broadband optical spectra and enhanced fiber-coupled output power. The LN-MLL, employing a high-reflectivity TFLN mirror and a high-reflectivity facet on the RSOA, produces a stable broadband frequency comb spanning 45 nm, with a notable 10-dB spectral bandwidth of 19.1 nm and a stable mode-locking beat note SNR exceeding 60 dB. The RSOA-MLL, designed with a low-reflectivity mirror on the RSOA chip, achieves significantly higher off-chip output power (up to 26 mW) with a 10-dB bandwidth of 11.4 nm, effectively alleviating coupling-loss limitations inherent to TFLN integrated photonic platforms. Experimental results indicate that the spectral bandwidth increases with the driving current, primarily because the RSOA gain spectrum broadens with increasing current. Numerical analysis based on HME and GNLSE models clarifies that the coexistence of homogeneous and inhomogeneous gain components within the RSOA plays a significant role in effectively overcoming dispersion-induced bandwidth limitations and facilitating broadband comb generation. The demonstrated dissipative mode-locking state allows broadband spectral generation in cavities with relatively large dispersion, without requiring near-zero dispersion engineering.

This work reveals the potential of III-V/TFLN integrated actively mode-locked lasers for chip-scale OFC technologies, particularly for broadband, high-power applications in optical communications, LiDAR, and metrology. Furthermore, the TFLN platform supports the integration of diverse nonlinear optical functionalities [51], including supercontinuum generation [52], pulse compression [53], and second-harmonic generation [54–56]. The integrated actively mode-locked lasers demonstrated in this work provide a feasible approach toward realizing chip-scale OFC sources compatible with these functionalities, creating new opportunities for advanced integrated photonic systems [57, 58], and enabling scalable solutions for a broad range of applications.

6 | Method

6.1 | Device Fabrication

The devices are fabricated on a 600-nm-thick X-cut magnesium oxide (MgO)-doped TFLN. The nanowaveguide structures are patterned using electron beam lithography and defined through an Ar-ion milling process, with an etching depth of 300 nm. The Sagnac loop reflectors incorporate directional couplers with a waveguide width of 1 μm, a coupling gap of 800 nm, and coupling lengths of 15 and 25 μm, corresponding to reflection

ratios of approximately 70% and 96%, respectively. An 800-nm-thick SiO_2 cladding layer is deposited over the entire chip, after which electrode windows are defined using UV photolithography. Subsequently, 800-nm-thick gold electrodes are formed via UV photolithography and electron-beam evaporation. The phase modulation features a length of 6.5 mm, with an electrode gap of 5 μm and a waveguide width of 1.4 μm.

Acknowledgements

We acknowledge the Center for Advanced Electronic Materials and Devices (AEMD) of Shanghai Jiao Tong University for the sample fabrication support.

Funding

The National Natural Science Foundation of China (NSFC) (62405184), Science and Technology Commission of Shanghai Municipality (24JD1401700), and the Natural Science Foundation of Shanghai (24ZR1431400).

Conflicts of Interest

The authors declare no conflicts of interest.

Data Availability Statement

The data that support the findings of this study are available from the corresponding author upon reasonable request.

References

1. P. Marin-Palomo, J. N. Kemal, M. Karpov, et al., "Microresonator-Based Solitons for Massively Parallel Coherent Optical Communications," *Nature* 546 (2017): 274–279, https://doi.org/10.1038/nature22387.

2. A. Rizzo, A. Novick, V. Gopal, et al., "Massively Scalable Kerr Comb-driven Silicon Photonic Link," *Nature Photonics* 17 (2023): 781–790, https://doi.org/10.1038/s41566-023-01244-7.

3. Y. Liu, H. Zhang, J. Liu, et al., "Parallel Wavelength-Division-Multiplexed Signal Transmission and Dispersion Compensation Enabled by Soliton Microcombs and Microrings," *Nature Communications* 15 (2024): 3645, https://doi.org/10.1038/s41467-024-47904-2.

4. D. T. Spencer, T. Drake, T. C. Briles, et al., "An Optical-Frequency Synthesizer Using Integrated Photonics," *Nature* 557 (2018): 81–85, https://doi.org/10.1038/s41586-018-0065-7.

5. N. Singh, M. Xin, N. Li, et al., "Silicon Photonics Optical Frequency Synthesizer," *Laser & Photonics Reviews* 14 (2020): 1900449, https://doi.org/10.1002/lpor.201900449.

6. P. Trocha, M. Karpov, D. Ganin, et al., "Ultrafast Optical Ranging Using Microresonator Soliton Frequency Combs," *Science* 359 (2018): 887–891, https://doi.org/10.1126/science.aao3924.

7. J. Riemensberger, A. Lukashchuk, M. Karpov, et al., "Massively Parallel Coherent Laser Ranging Using a Soliton Microcomb," *Nature* 581 (2020): 164–170, https://doi.org/10.1038/s41586-020-2239-3.

8. Y.-S. Jang, H. Ahn, S. Eom, J. Park, and J. Jin, "Approaching the Quantum-Limited Precision in Frequency-Comb-Based Spectral Interferometric Ranging," *Laser & Photonics Reviews* 19 (2025): 2401995, https://doi.org/10.1002/lpor.202401995.

9. N. Picqué and T. W. Hänsch, "Frequency Comb Spectroscopy," *Nature Photonics* 13 (2019): 146–157.

10. L. A. Sterczewski and M. Bagheri, "Sub-Nominal Resolution Fourier Transform Spectrometry with Chip-Based Combs," *Laser & Photonics Reviews* 18 (2024): 2300724, https://doi.org/10.1002/lpor.202300724.

11. E. Obrzud, M. Rainer, A. Harutyunyan, et al., "A Microphotonic Astrocomb," *Nature Photonics* 13 (2019): 31–35, https://doi.org/10.1038/s41566-018-0309-y.

12. M.-G. Suh, X. Yi, Y.-H. Lai, et al., "Searching for Exoplanets Using a Microresonator Astrocomb," *Nature Photonics* 13 (2019): 25–30, https://doi.org/10.1038/s41566-018-0312-3.

13. J. Feldmann, N. Youngblood, M. Karpov, et al., "Parallel Convolutional Processing Using an Integrated Photonic Tensor Core," *Nature* 589 (2021): 52–58, https://doi.org/10.1038/s41586-020-03070-1.

14. S. Chen, Y. Zheng, Y. Xu, et al., "High-Bit-Efficiency TOPS Optical Tensor Convolutional Accelerator Using Microcombs," *Laser & Photonics Reviews* 19 (2025): 2401975, https://doi.org/10.1002/lpor.202401975.

15. J. Liu, E. Lucas, A. S. Raja, et al., "Photonic Microwave Generation in the X- and K-band Using Integrated Soliton Microcombs," *Nature Photonics* 14 (2020): 486–491, https://doi.org/10.1038/s41566-020-0617-x.

16. W. Sun, Z. Chen, L. Li, et al., "A Chip-integrated Comb-Based Microwave Oscillator," *Light: Science & Applications* 14 (2025): 179, https://doi.org/10.1038/s41377-025-01795-0.

17. L. Huang, C. Yang, L. Liang, et al., "Integrated Light Sources Based on Micro-Ring Resonators for Chip-Based LiDAR," *Laser & Photonics Reviews* 19 (2025): 2400343, https://doi.org/10.1002/lpor.202400343.

18. Y. Sun, J. Wu, M. Tan, et al., "Applications of Optical Microcombs," *Advances in Optics and Photonics* 15 (2023): 86–175, https://doi.org/10.1364/AOP.470264.

19. T. J. Kippenberg, A. L. Gaeta, M. Lipson, and M. L. Gorodetsky, "Dissipative Kerr Solitons in Optical Microresonators," *Science* 361 (2018): aan8083, https://doi.org/10.1126/science.aan8083.

20. A. Moscoso-Mártir, A. Tabatabaei-Mashayekh, J. Müller, et al., "8-channel WDM Silicon Photonics Transceiver with SOA and Semiconductor Mode-locked Laser," *Optics Express* 26 (2018): 25446–25459, https://doi.org/10.1364/OE.26.025446.

21. T. Verolet, G. Aubin, Y. Lin, et al., "Mode Locked Laser Phase Noise Reduction under Optical Feedback for Coherent DWDM Communication," *Journal of Lightwave Technology* 38 (2020): 5708–5715, https://doi.org/10.1109/JLT.2020.3002653.

22. J. Qin, J. Huang, B. Yang, Z. Wang, T. Wang, and J. Zhang, "Ultra-Reliable Quantum Dot Colliding Pulse Mode-locked Laser as Multi-Wavelength Source for Integrated Optical Interconnects," *Optics Express* 32 (2024): 9095–9104, https://doi.org/10.1364/OE.515398.

23. S. Pan, V. Cao, Y. Feng, et al., "Highly Reliable, Ultra-Wideband 100 GHz Quantum-Dot Mode-Locked Frequency Combs for O-Band Terabit Optical Interconnects," *Laser & Photonics Reviews* (2025): e01559, https://doi.org/10.1002/lpor.202501559.

24. D. J. Derickson, R. J. Helkey, A. Mar, J. R. Karin, J. G. Wasserbauer, and J. E. Bowers, "Short Pulse Generation Using Multisegment Mode-locked Semiconductor Lasers," *IEEE Journal of Quantum Electronics* 28 (1992): 2186–2202, https://doi.org/10.1109/3.159527.

25. S. Liu, J. C. Norman, D. Jung, M. J. Kennedy, A. C. Gossard, and J. E. Bowers, "Monolithic 9 GHz Passively Mode Locked Quantum Dot Lasers Directly Grown on on-axis (001) Si," *Applied Physics Letters* 113 (2018): 041108.

26. M. L. Davenport, S. Liu, and J. E. Bowers, "Integrated Heterogeneous Silicon/III–V Mode-locked Lasers," *Photonics Research* 6 (2018): 468–478, https://doi.org/10.1364/PRJ.6.000468.

27. S. Liu, X. Wu, D. Jung, et al., "High-Channel-Count 20 GHz Passively Mode-Locked Quantum Dot Laser Directly Grown on Si with 41 Tbit/s Transmission Capacity," *Optica* 6 (2019): 128–134, https://doi.org/10.1364/OPTICA.6.000128.

28. M. Shekarpour and M. H. Yavari, "Timing Jitter Reduction of Silicon Hybrid Harmonically Mode-locked Ring Laser Using an Integrated Sampled-grating DBR," *Optics Letters* 47 (2022): 2016–2019, https://doi.org/10.1364/OL.452246.

29. A. Hermans, K. Van Gasse, J. Ø. Kjellman, et al., "High-Pulse-Energy III-V-on-Silicon-Nitride Mode-Locked Laser," *APL Photonics* 6 (2021): 096102, https://doi.org/10.1063/5.0058022.

30. E. Vissers, S. Poelman, C. O. de Beeck, K. Van Gasse, and B. Kuyken, "Hybrid Integrated Mode-Locked Laser Diodes with a Silicon Nitride Extended Cavity," *Optics Express* 29 (2021): 15013–15022, https://doi.org/10.1364/OE.422621.

31. S. Cuyvers, B. Haq, C. Op de Beeck, et al., "Low Noise Heterogeneous III-V-on-Silicon-Nitride Mode-Locked Comb Laser," *Laser & Photonics Reviews* 15 (2021): 2000485, https://doi.org/10.1002/lpor.202000485.

32. E. Vissers, S. Poelman, H. Wenzel, et al., "Hybrid Integrated Mode-locked Laser Using a GaAs-based 1064 Nm Gain Chip and a SiN External Cavity," *Optics Express* 30 (2022): 42394–42405, https://doi.org/10.1364/OE.474671.

33. L. Chang, S. Liu, and J. E. Bowers, "Integrated Optical Frequency Comb Technologies," *Nature Photonics* 16 (2022): 95–108, https://doi.org/10.1038/s41566-021-00945-1.

34. Q. Guo, B. K. Gutierrez, R. Sekine, et al., "Ultrafast Mode-Locked Laser in Nanophotonic Lithium Niobate," *Science* 382 (2023): 708–713, https://doi.org/10.1126/science.adj5438.

35. J. Ling, Z. Gao, S. Xue, et al., "Electrically Empowered Microcomb Laser," *Nature Communications* 15 (2024): 4192, https://doi.org/10.1038/s41467-024-48544-2.

36. D. Kuizenga and A. Siegman, "FM and AM Mode Locking of the Homogeneous Laser—Part II: Experimental Results in a Nd:YAG Laser with Internal FM Modulation," *IEEE Journal of Quantum Electronics* 6 (1970): 709–715, https://doi.org/10.1109/JQE.1970.1076344.

37. N. G. Usechak, G. P. Agrawal, and J. D. Zuegel, "FM Mode-Locked Fiber Lasers Operating in the Autosoliton Regime," *IEEE Journal of Quantum Electronics* 41 (2005): 753–761, https://doi.org/10.1109/JQE.2005.846695.

38. H. Haus, "A Theory of Forced Mode Locking," *IEEE Journal of Quantum Electronics* 11 (1975): 323–330, https://doi.org/10.1109/JQE.1975.1068636.

39. F. X. Kärtner, D. Kopf, and U. Keller, "Solitary-Pulse Stabilization and Shortening in Actively Mode-Locked Lasers," *Journal of the Optical Society of America B* 12 (1995): 486–496, https://doi.org/10.1364/JOSAB.12.000486.

40. L. A. Coldren, S. W. Corzine, and M. L. Mašanović, "Gain and Current Relations," in *Diode Lasers and Photonic Integrated Circuits* (John Wiley & Sons, 2012), https://doi.org/10.1002/9781118148167.

41. M. Sugawara, T. Fujii, M. Kondo, et al., "Evaluation of Exciton Absorption Peak Broadening Factors in InGaAsP/InP Multiple Quantum Wells," *Applied Physics Letters* 53 (1988): 2290–2292, https://doi.org/10.1063/1.100256.

42. T. Takahashi and Y. Arakawa, "Nonlinear Gain Effects in Quantum Well, Quantum Well Wire, and Quantum Well Box Lasers," *IEEE Journal of Quantum Electronics* 27 (1991): 1824–1829, https://doi.org/10.1109/3.90011.

43. F. Quinlan, S. Gee, S. Ozharar, and P. Delfyett, "The Effects of Filtering RF Source Phase Noise by a Low Noise, High Quality Factor Actively Modelocked Laser on the Laser's Absolute and Relative Phase Noise," *Optics Express* 14 (2006): 5346–5355, https://doi.org/10.1364/OE.14.005346.

44. J. Huang and L. W. Casperson, "Gain and Saturation in Semiconductor Lasers," *Optical and Quantum Electronics* 25 (1993): 369–390, https://doi.org/10.1007/BF00420579.

45. G. P. Agrawal and N. K. Dutta, "Basic Concepts," in *Semiconductor Lasers*, ed. G. P. Agrawal, and N. K. Dutta, (Springer US, 1993), https://doi.org/10.1007/978-1-4613-0481-4.

46. L. He, M. Zhang, A. Shams-Ansari, R. Zhu, C. Wang, and L. Marko, "Low-Loss Fiber-to-Chip Interface for Lithium Niobate Photonic Integrated Circuits," *Optics Letters* 44 (2019): 2314–2317, https://doi.org/10.1364/OL.44.002314.

47. C. Hu, A. Pan, T. Li, et al., "High-efficient Coupler for Thin-Film Lithium Niobate Waveguide Devices," *Optics Express* 29 (2021): 5397–5406, https://doi.org/10.1364/OE.416492.

48. D. Jia, Q. Luo, C. Yang, et al., "High-Efficiency Edge Couplers Enabled by Vertically Tapering on Lithium-Niobate Photonic Chips," *Applied Physics Letters* 123 (2023): 263502, https://doi.org/10.1063/5.0184899.

49. G. Chen, K. Chen, Z. Yu, and L. Liu, "Low-loss and Broadband Polarization-diversity Edge Coupler on a Thin-film Lithium Niobate Platform," *Optics Letters* 48 (2023): 4145–4148, https://doi.org/10.1364/OL.494891.

50. H. K. Tsang, R. V. Penty, I. H. White, et al., "Two-Photon Absorption and Self-phase Modulation in InGaAsP/InP Multi-Quantum-well Waveguides," *Journal of Applied Physics* 70 (1991): 3992–3994, https://doi.org/10.1063/1.349168.

51. M. G. Vazimali and S. Fathpour, "Applications of Thin-Film Lithium Niobate in Nonlinear Integrated Photonics," *Advanced Photonics* 4 (2022): 034001, https://doi.org/10.1117/1.AP.4.3.034001.

52. T.-H. Wu, L. Ledezma, C. Fredrick, et al., "Visible-to-Ultraviolet Frequency Comb Generation in Lithium Niobate Nanophotonic Waveguides," *Nature Photonics* 18 (2024): 218–223, https://doi.org/10.1038/s41566-023-01364-0.

53. M. Yu, D. Barton III, R. Cheng, et al., "Integrated Femtosecond Pulse Generator on Thin-film Lithium Niobate," *Nature* 612 (2022): 252–258, https://doi.org/10.1038/s41586-022-05345-1.

54. J. Lu, J. B. Surya, X. Liu, et al., "Periodically Poled Thin-Film Lithium Niobate Microring Resonators with a Second-Harmonic Generation Efficiency of 250,000%/W," *Optica* 6 (2019): 1455–1460, https://doi.org/10.1364/OPTICA.6.001455.

55. P.-K. Chen, I. Briggs, C. Cui, L. Zhang, M. Shah, and L. Fan, "Adapted Poling to Break the Nonlinear Efficiency Limit in Nanophotonic Lithium Niobate Waveguides," *Nature Nanotechnology* 19 (2024): 44–50, https://doi.org/10.1038/s41565-023-01525-w.

56. L. Qu, W. Wu, W. Cai, M. Ren, and J. Xu, "Second Harmonic Generation in Lithium Niobate on Insulator," *Laser & Photonics Reviews* 19 (2025): 2401928, https://doi.org/10.1002/lpor.202401928.

57. D. Zhu, L. Shao, M. Yu, et al., "Integrated Photonics on Thin-Film Lithium Niobate," *Advances in Optics and Photonics* 13 (2021): 242–352, https://doi.org/10.1364/AOP.411024.

58. Z. Xie, B. Fang, L. Jintian, et al., "Recent Development in Integrated Lithium Niobate Photonics," *Advances in Physics: X* 9 (2024): 2322739.

Appendix A: Values of Parameters used in the Simulation of Figure 2

Parameter	Value	Unit
g_0	2.3	/
P_{sat}	−7	dBm
λ_0	1620	nm
T_R	147	ps
l	0.98	/
Δf_g	5	THz
D	2000	fs^2
M	π	/
f_m	6.8	GHz

Appendix B: Values of Parameters used in the Simulation of Figure 6

Parameter	Value	Unit
TFLN nanowaveguide propagation loss	1.5	dB/cm
Single-pass small-signal gain of RSOA	20	dB
Coupling loss between TFLN and RSOA chips	2	dB
Length of the RSOA	1	mm
Length of the TFLN nanowaveguide	8.2	mm
Fraction of inhomogeneous gain	1.5%	/
TFLN nanowaveguide dispersion	100	ps^2/km
RSOA waveguide dispersion	1200	ps^2/km
Mode area of TFLN nanowaveguide	0.93	μm^2
Mode area of RSOA waveguide	8	μm^2
Modulation frequency	6.8	GHz
Modulation depth	π	/